Remote Sens. **2011**, *3*, 684-707; doi:10.3390/rs3040684

OPEN ACCESS

Remote Sensing

ISSN 2072-4292

www.mdpi.com/journal/remotesensing

Article

MERIS Retrieval of Water Quality Components in the Turbid Albemarle-Pamlico Sound Estuary, USA

Leonid G. Sokoletsky [1], Ross S. Lunetta [2,*], Michael S. Wetz [1,†] and Hans W. Paerl [3]

[1] National Exposure Research Laboratory, US Environmental Protection Agency, National Research Council, 109 TW Alexander Dr., Research Triangle Park, NC 27711, USA; E-Mails: sokoletsky.leonid@gmail.com (L.G.S.); michael.wetz@tamucc.edu (M.S.W.)

[2] National Exposure Research Laboratory, US Environmental Protection Agency, 109 TW Alexander Dr., Research Triangle Park, NC 27711, USA

[3] Institute of Marine Sciences, University of North Carolina at Chapel Hill, Morehead City, NC 28557, USA; E-Mail: hpaerl@email.unc.edu

* Author to whom correspondence should be addressed; E-Mail: lunetta.ross@epa.gov; Tel.: +1-919-541-4256.

† Present Affiliation: Department of Life Sciences, Texas A&M University-Corpus Christi, Corpus Christi, TX 78412, USA.

Received: 1 February 2011; in revised form: 14 March 2011 / Accepted: 18 March 2011 / Published: 1 April 2011

Abstract: Two remote-sensing optical algorithms for the retrieval of the water quality components (WQCs) in the Albemarle-Pamlico Estuarine System (APES) were developed and validated for chlorophyll *a* (Chl). Both algorithms were semi-empirical because they incorporated some elements of optical processes in the atmosphere, water, and air/water interface. One incorporated a very simple atmospheric correction and modified quasi-single-scattering approximation (QSSA) for estimating the spectral Gordon's parameter, and the second estimated WQCs directly from the top of atmosphere satellite radiance without atmospheric corrections. A modified version of the Global Meteorological Database for Solar Energy and Applied Meteorology (METEONORM) was used to estimate directional atmospheric transmittances. The study incorporated *in situ* Chl data from the Ferry-Based Monitoring (FerryMon) program collected in the Neuse River Estuary (n = 633) and Pamlico Sound (n = 362), along with Medium Resolution Imaging Spectrometer (MERIS) satellite imagery collected (2006–2009) across the APES; providing quasi-coinciding samples for Chl algorithm development and validation. Results

indicated a coefficient of determination (R^2) of 0.70 and mean-normalized root-mean-squares errors (NRMSE) of 52% in the Neuse River Estuary and R^2 = 0.44 (NRMSE = 75 %) in the Pamlico Sound—without atmospheric corrections. The simple atmospheric correction tested provided on performance improvements. Algorithm performance demonstrated the potential for supporting long-term operational WQCs satellite monitoring in the APES.

Keywords: water quality; optical retrieval algorithms; MERIS imagery; estuary system

1. Introduction

Ocean color was first measured from space in 1979 and has since provided a synoptic view of near-surface water quality components (WQCs) like chlorophyll *a* (Chl), volatile suspended solids (VSS), fixed suspended solids (FSS), total suspended solids (TSS), and absorption of chromophoric dissolved organic matter (a_{CDOM}). Subsequently, a number of ocean color satellite missions have been used to monitor phytoplankton biomass and other biogeochemical variables across temporal (daily to annual) and spatial (kilometers to ocean basin) scales [1]. Numerous satellite remote-sensing empirical and semi-empirical algorithms for water color retrieval (especially for oceanic phytoplankton) have been created during this time [2–4].

An extensive list of remote sensing methods for estimation of inherent optical properties (IOPs) including absorption (a) and backscattering (b_b) coefficients have been reported by the International Ocean-Colour Coordinating Group [5]. However, to date, most methods have been developed for Case 1 waters, where upwelling radiance is mostly associated with phytoplankton pigments. In turbid Case 2 waters, the upwelling signal is frequently associated with multiple constituents (including TSS and CDOM) and is substantially complicated due to lack of significant correlation among WQCs.

Attempts to develop remote sensing algorithms for water quality assessment in the NRE (Neuse River Estuary) and Pamlico Sound (PS) began in the mid-1980s. The Multispectral Scanner (MSS) carried by Landsats 1–5 was the first satellite sensor used to assess NRE WQCs including salinity, Chl, turbidity and TSS [6]. The authors noted that the NRE "began to exhibit symptoms of degradation similar to those seen in other estuaries." An important study contribution was the determination of NRE bottom reflectance impacts on modeling feasibility. Khorram and Cheshire [6] concluded that bottom reflectance was significant at depths Z < 3 m and remote sensing-derived WQCs were well correlated with *in situ* measurements for the depths Z > 3 m. For example, the coefficient of determination (R^2) was 0.70 and 0.76 for Chl and turbidity (n = 17), respectively; 0.82 for salinity and 0.64 for TSS (n = 45). However, these models were completely empirical and had a high probability for substantial error propagation.

Woodruff *et al.* [7] measured mean diffuse attenuation coefficients in the visible region K_d(PAR) ranging 0.7–2.9 (mean 1.3) m^{-1} in the NRE and ranging from 0.5 to 2.7 (mean 1.0) m^{-1} in the PS. Woodruff *et al.* [7] estimated K_d(PAR) and TSS in PS using a simplified modification [8] of the quasi-single-scattering approximation (QSSA) [9]. According to the model described in [7], the irradiance reflectance was only a function of the Gordon's parameter $G = b_b/(b_b + a)$. No scattering

phase function or geometry of illumination and observation were taken into account. However, as shown by Haltrin and Gallegos [10] and Sokoletsky [11], neglecting these factors may lead to large errors. Additionally, it was assumed [7] that the specific absorption and backscattering coefficients for PS were constants. This assumption is probably not valid for the NRE and PS area of interest due to the large variability of dissolved and suspended matter in the water resulting in different optical responses [12–14]. Nevertheless, the relationship between reflectance in the red region (580–680 nm) and K_d(PAR) in PS was fairly robust (R^2 = 0.72; n = 61) under a variety of environmental conditions [8].

Karaska *et al.* [15] mapped WQCs (Chl, TSM, CDOM and total attenuation) in the NRE using the photobathymetry and water quality software presented by Huguenin *et al.* [16]. The software was based on a four-dimensional look-up-table (LUT) representing irradiance reflectance as a function of wavelength, depth, and concentrations of Chl, TSM and CDOM using the Morel and Prieur [17] model modified for shallow (finite) layers. Both [15] and [16] did not account for the important impacts of scattering phase function, illumination and observation geometry and variability of the specific absorption and backscattering coefficients. The results for the Advanced Visible-Infrared Imaging Spectrometer (AVIRIS) derived Chl using the above-mentioned approach for eight southeastern Massachusetts lakes was a R^2 = 0.89, while the relative errors varied from −64% to 207%; with a mean-normalized root-mean-squares error (NRMSE) of 74% [16]. Improved results were achieved by this approach for Chl retrieval along three NRE transects when the elapsed time Δt between the field data and the AVIRIS data collection was within one hour (R^2 = 0.67, 0.76 and 0.90); at Δt > 2 h results were not acceptable [15].

The application of spectral radiance ratios or spectral reflectance ratios largely removes angular scattering features, geometrical factors and bottom influence effects from the solution, and flattens the non-linear behavior of reflectance as a function of Gordon's parameter G [3,4,18–23], thus improving IOPs retrievals and WQCs estimates. Several authors have modified a spectral reflectance ratio empirical method for development of various variants of adaptive optical algorithms for IOPs and WQCs estimation [4,24–30]. Like the reflectance ratio approach, adaptive optical algorithms can overcome ambiguousness of IOPs estimations from known reflectance [31].

Lunetta *et al.* [32] were able to estimate Chl, CDOM, TSS and FSS for the NRE and PS using atmospherically corrected (radiative transfer model) narrow band (9.5 nm) surface reflectance $R(\lambda)$ or $R(\lambda)$ ratios to estimate WQCs. The spectral bands and ratios represented a subset of AVIRIS bands that were selected to simulate both the Moderate Resolution Imaging Spectroradiometer (MODIS) and Medium Resolution Imaging Spectrometer (MERIS) sensors. Atmospheric correction used LUTs generated using the MODerate resolution atmospheric TRANsmission (MODTRAN) radiative transfer model for calculation of upwelling spectral radiances corresponding to the range of surface reflectances, atmospheric aerosol loadings and water vapor that would anticipate the range of observed radiances in the study region [33]. The MODTRAN code uses a discrete ordinate method for solution of the radiative transfer equation [34]. The best surface reflectance indices were found as follows (sample size n = 13): R(693)/R(673) for Chl (R^2 = 0.98); R(470)/R(555) for CDOM (R^2 = 0.90); and R(620–670) for TSS (R^2 = 0.55) and FSS (R^2 = 0.64). Thus, the significance levels (p) for all above-mentioned WQCs were p < 0.003 and results considered statistically significant. A quantification of VSS did not produce acceptable results.

Sokoletsky *et al.* [30] developed a semi-empirical underwater optical algorithm for WQCs in NRE and PS using Gordon's parameter spectral ratios instead of reflectance spectral ratios. The authors used $G(665)/G(560)$ spectral ratios for $a_{CDOM}(412.5)$ estimation and $G(709)/G(665)$ for Chl, $a_{TSS}(665)$, TSS, VSS and FSS retrievals. Determination coefficients between the algorithm-derived and *in situ* measured WQCs were 0.88 (n = 79) for Chl, 0.59 (n = 79) for $a_{CDOM}(412.5)$, 0.51 (n = 68) for TSS, 0.78 (n = 68) for VSS, and 0.00 (n = 68) for FSS; demonstrating highly significant results for all WQCs investigated, excluding FSS. This was similar to results by Khorram and Cheshire [6], Karaska *et al.* [15] for Chl estimation and Lunetta *et al.* [32] for Chl, CDOM and TSS. However, the different results obtained for VSS and FSS in [30] and [32] can be attributed to the distinctive seasonal data. For example, all measurements used for WQCs retrieval in [32] were limited to one day and small sample size (n = 13); while the results reported in [30] were based on nine observation dates (n = 79).

1.1. Study Area

The NRE is the largest tributary of the North Carolina's Albemarle-Pamlico Estuarine System (APES) which is the second largest estuarine complex in the USA. This complex is representative of shallow, periodically stratified, semi-lagoonal estuaries, found along the Mid-Atlantic. The NRE drains some of North Carolina's most productive agricultural land and rapidly expanding urban areas. The NRE originates in the piedmont of North Carolina, near Durham, flows through Raleigh and empties into the PS beyond New Bern (Figure 1). The NRE is approximately 325 km in length, with depths between 2 and 7 m, averaging approximately 7.5 m in the Northern Pamlico basin. The Neuse River is among the widest in the USA; ranging from 2 km at New Bern to 12 km at the PS confluence [35–37]. The APES supports approximately 80% of commercially and recreationally-caught coastal fisheries species in the Southeastern Atlantic Region [38]. Over the past several decades, this system has been adversely affected by human activities (*i.e.*, changes in nutrient loadings and habitat degradation) and climatic perturbations, including a recent increase in tropical cyclones [35,36]. These factors have led to degradation of water/habitat quality, and have caused declines of fisheries resources and of overall ecological condition [35,36,39,40].

The NRE is an example of a water body belonging to the intermediate water case with: (a) significant quantities of Chl, organic and inorganic matter; (b) predictable relationships between Chl, VSS and TSS; and (c) no strong correlations between Chl, FSS and CDOM [30]. Diffuse attenuation coefficients across the visible range, $K_d(PAR)$, typically range from 1.0 m^{-1} to 2.5 m^{-1} in the NRE-PS region [7]; therefore, the diffuse attenuation optical depth $\tau_k(PAR) = ZK_d(PAR)$ ranges from 2 to 18.

Figure 1. The Neuse River-Pamlico Sound Estuarine System including ModMon stations and FerryMon routes.

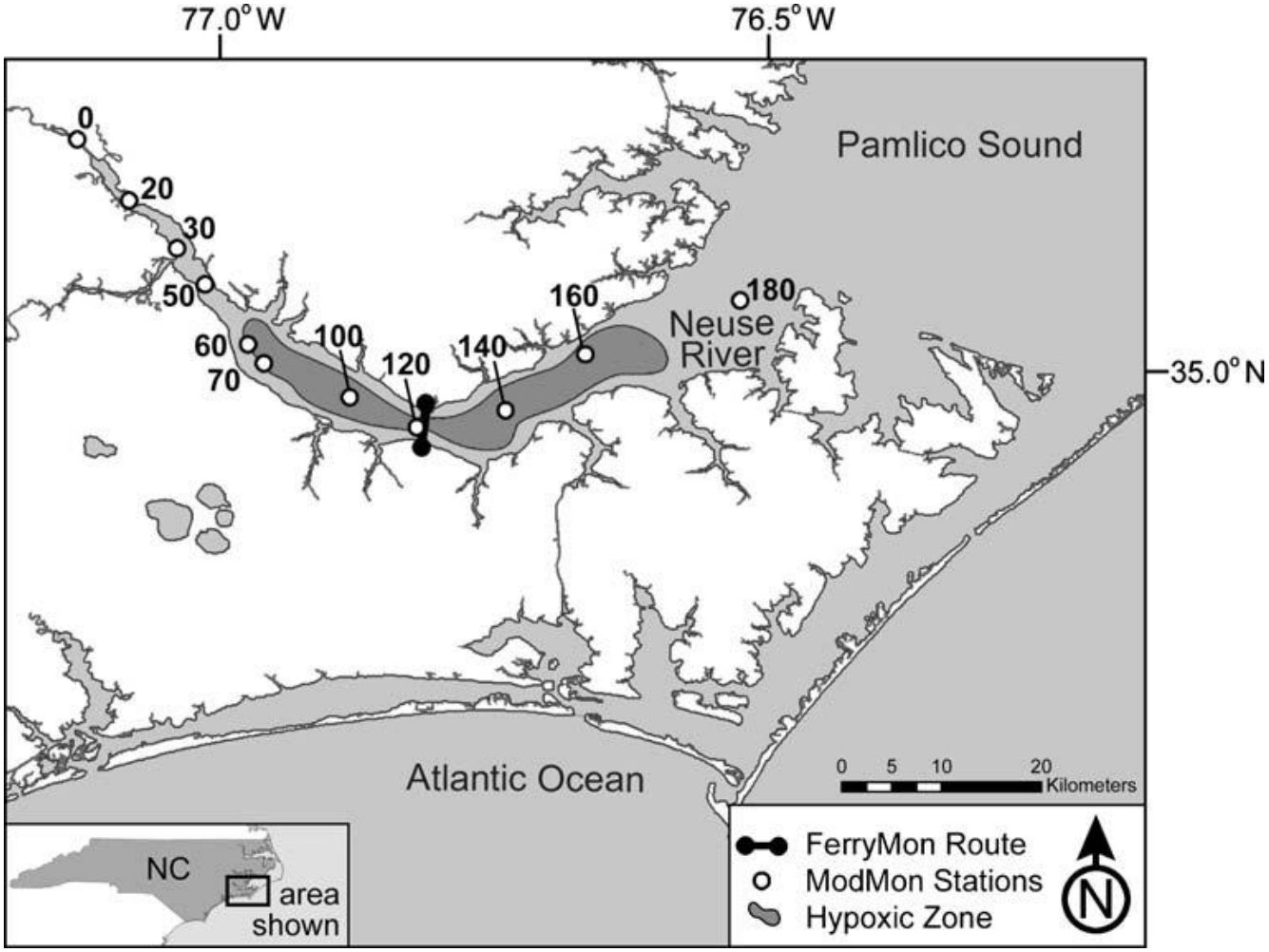

2. Methods

In this study we developed two different variants for WQCs retrieval in the NRE and PS. One algorithm used a very simplistic atmospheric correction to derive spectral values of surface reflectance and surface Gordon's parameter $G(\lambda, 0-)$ at λ = 665 and 709 nm; while the second algorithm did not incorporate any atmospheric correction and was based on the top of atmosphere (TOA) radiance values measured at sensor (Figure 2). Both algorithms were developed for NRE and validated for the NRE (n = 633) and PS (n = 362) areas. For assessment of TSS, VSS, FSS and CDOM WQCs, the Neuse River Estuary Modeling and Monitoring Project (ModMon) data collection also was exploited [30].

2.1. Radiometric Measurements

Radiometric data collections using a Satlantic Hyper Pro profiling instrument were performed in conjunction with the NRE Modeling and Monitoring Project (ModMon) [41]. The modified ModMon protocols were used to collect radiometric data as well as turbidity, Chl, CDOM, VSS, FSS.

Figure 2. Flow chart illustrating the algorithm development approach and validation procedures used in support of the study. Abbreviations: WQCs, water quality components; NRE, Neuse River Estuary; PS, Pamlico Sound, TOA, top of atmosphere.

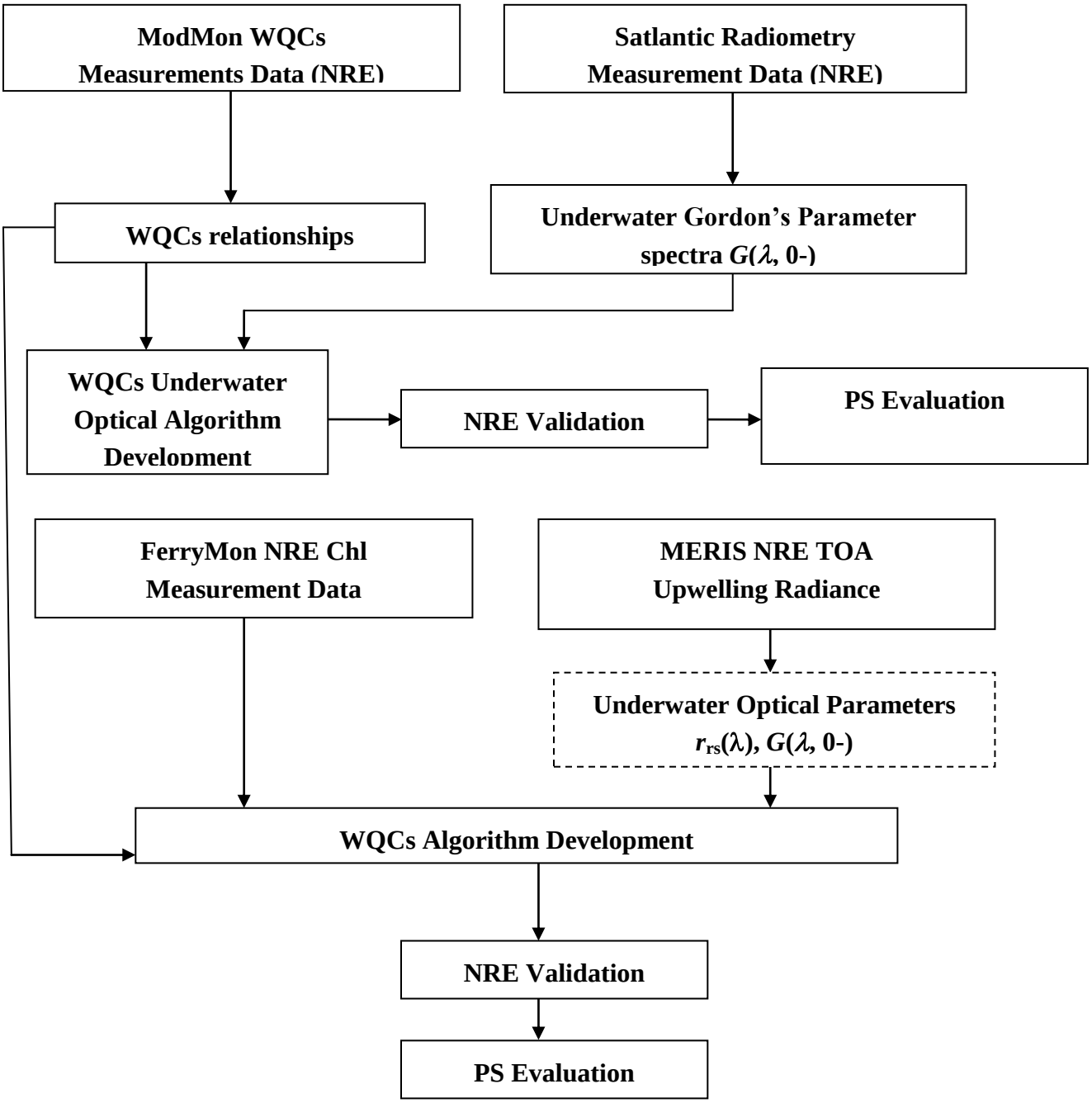

TSS, diffuse attenuation coefficient, temperature and salinity data at 10 stations for nine dates within the 2006–2009 study duration (Figure 1). All radiometric measurements were acquired during morning hours, at zero nadir viewing angles. These measurements included spectra from 350 to 800 nm with a mean band width of 3.3 nm. Both downwelling irradiance just above the water $E_d(\lambda, 0+)$ and underwater upwelling radiance $L_u(\lambda, z)$ at depth z were collected. Measurements were made in the vertical plane normal to the Sun's azimuthal plane to minimize the contribution effects of sun glitter and of ship shadowing [42].

The photosynthetically available radiation K_d(PAR) and the corresponding diffuse attenuation optical depth τ_k(PAR) were averaged from the surface to the bottom depth. K_d(PAR) was calculated from PAR measured in the i^{th} layer (n = 547). The ranges of K_d(PAR) and τ_k(PAR) were estimated at [0.5;3.3] m^{-1} and [2.5;10.5] with a mean of 1.6 (±0.5) m^{-1} and 6.0 (±1.5), respectively, for all NRE stations. Accounting for a "semi-infinite" layer at τ_k(PAR) > 2.5 − 3 [43], we ignored the bottom's influence on the optical surface measurements in the APES. Note, the similarity of the K_d(PAR) data in this study to that reported in [7].

2.2. Water Quality Measurements

Relevant parameters determined as part of ModMon included vertical profiles of PAR, temperature, salinity, Chl fluorescence, and turbidity at 0.5 m depth intervals for each sampling location. Discrete samples for VSS (n = 68), FSS (n = 68), TSS (n = 68), Chl (n = 79), and $a_{CDOM}(\lambda)$ (n = 79) were also collected at near-surface and bottom at each site. To support underwater optical model development, only subsurface values of WQCs were used. Experimental methods of WQCs determination used in the study are described in [30].

An additional dataset of near-surface Chl measurements was obtained through the North Carolina Ferry-Based Monitoring (FerryMon) Program; which consisted of two NC Department of Transportation ferries, traversing both the NRE and PS. The NRE ferry completed 40 crossings daily between Cherry Point and Minnesott Beach, while the PS ferry completed four daily crossings between Cedar Island and Ocracoke Island (Figure 1). The FerryMon database included 142,265 NRE and 173,918 PS Chl measurement observations from 2006 to 2009. Ferries were equipped with automated water quality monitoring systems, including a flow-through YSI 6600 sondes that measured Chl fluorescence, conductivity, turbidity, temperature, salinity, dissolved oxygen and pH [41,44]. *In vivo* fluorescence was converted to Chl concentrations according to calibration equations relating fluorescence to various concentrations of extracted Chl. The random error associated with the fluorometric Chl determinations for both the ModMon and FerryMon programs was estimated using parallel laboratory measurement protocols. A systematic error of approximately 2.0% associated with the ferry-based estimates was minimized by regular calibrations.

2.3. Satellite Imagery

We used the Medium Resolution Imaging Spectrometer (MERIS) for its relatively high spatial resolution and spectral bands optimized for estimating WQCs. In particular, the 704–713 nm band was previously determined to be extremely important for APES water quality monitoring [32,45]. MERIS was designed by the European Space Agency (ESA) for ocean and coastal water remote sensing applications. The MERIS design features include a spatial resolution of 300 m (high resolution mode) together with a revisit period of 2–3 days (latitude dependent), 15 narrow spectral bands in the 400–900 nm spectral range with a relatively high signal to noise ratio, high radiometric sensitivity and stability, and radiometric errors < 2% [45]. MERIS was launched into a sun synchronous polar orbit onboard the ESA's Environmental Satellite 1 (EnviSat-1) on 1 March 2002. It was deployed as a research instrument with an initial mission cycle scheduled through 2010; which has subsequently

been extended through 2013. A follow-on instrument is scheduled for deployment 2013 onboard ESA's Sentinel-2.

To achieve correspondence between the MERIS Chl retrievals and the FerryMon measurements, only those data aligned in both time ($\Delta t \leq 4$ h) and space ($\Delta d \leq 150$ m) were used for algorithm validation. The numerical test did not reveal any statistically significant differences between the radiance signals detected by the sensor at selected and diminished times and distances.

2.4. Water Quality Retrieval Algorithms

The MERIS upwelling TOA spectral radiance L_u(TOA, λ) and FerryMon data from the NRE was used to support algorithm development (n = 633). Auxiliary data such as nadir viewing angle of satellite's sensor, wind speed, atmospheric pressure, relative humidity, and ozone density (in Dobson units) were derived from the MERIS L1b images (N1 format) by the open-source toolbox BEAM-VISAT (version 4.5.2). The spectral scaling factors needed for conversion from the spectral TOA digital numbers to the spectral TOA upwelling radiance also were extracted using the toolbox. Detailed information about BEAM toolbox may be found at http://www.brockmann-consult.de/cms/web/beam/welcome.

Our modeling efforts revealed large uncertainties primarily attributed to the lack of aerosol properties information. Without additional information the development of a substantially complete version of atmospheric correction sub-algorithm was not possible [46–49]. Therefore, two approaches, one that incorporated a very simple atmospheric correction and one without any atmospheric correction were developed and tested. The flow chart for the development of algorithms used in the study is shown in Figure 2. Both algorithms incorporated NRE reflectance $r_{rs}(\lambda)$ values across three spectral regions corresponding to the minimum value at 650−676 nm (red) and two maximum values at 569−600 nm (green) and 683−710 nm (NIR) [30]. CDOM absorption was closely related to the green to red reflectance ratio, while Chl, VSS, and TSS concentrations were strongly influenced by the NIR to red reflectance ratio. The following equation for Chl (mg m^{-3}) algorithm with atmospheric correction was derived from the NRE FerryMon and MERIS data:

$$\text{Chl} = 20.28F^{3.854}, \quad F = \frac{1/G(665)-1}{1/G(709)-1} \tag{1}$$

This equation closely resembles that used in [30]. The function F was used to provide a more robust approach, compared to simple reflectance ratios or Gordon's parameter ratios.

Next, we incorporated an approximation equation relating $G(\lambda)$ with the surface spectral reflectance $r_{rs}(\lambda) = L_u(\lambda, 0-)/E_d(\lambda, 0-)$ ($L_u(\lambda, 0-)$ and $E_d(\lambda, 0-)$ that represents spectral upwelling radiance and downwelling irradiance, respectively:

$$r_{rs}(\lambda) = 0.2049G(\lambda)[1+0.2821G(\lambda)-1.019\mu_1+0.4561\mu_1^2](1+0.4021/\mu_2) \tag{2}$$

where μ_1 is the cosine of the subsurface solar zenith angle and μ_2 is the cosine of the subsurface nadir viewing angle. Equation (2) was derived based on results in [30] for the relationship between r_{rs}, and G and μ_1 incorporating $r_{rs}(\mu_2)$ relationship according to Albert and Gege [50]. The numerical calculations documented by [30] and [50] were based on the precise invariant imbedding method (IIM); however, basic assumptions used for r_{rs} model development were different. Details of our IIM computations are

outlined in [51–54]. The following assumptions were incorporated for derivation of Equation (2): (1) the strongly forward-peaked Fournier-Forand-Mobley (FFM) particulate scattering phase function; (2) solar zenith angles $\theta_0 \in [0°;61.7°]$; (3) nadir viewing angle $\theta_2 = 0°$; (4) wavelengths λ = {560 nm, 665 nm, 709 nm}; and (5) single-scattering albedo $\omega_0 \in [0.1;0.99]$. The FFM $p(\theta)$ was selected because it reproduces scattering conditions pertaining to different natural waters [55–57]. Equation (2) was then inverted as follows:

$$G(\lambda) = 1.773\left(\sqrt{F_1^2 + F_2(\lambda)} - F_1\right),\ F_1 = 1 - 1.019\mu_1 + 0.4561\mu_1^2,\ F_2(\lambda) = \frac{5.505 r_{rs}(\lambda)}{1 + 0.4021/\mu_2} \quad (3)$$

The atmospheric correction algorithm for conversion from the TOA spectral radiances to the above-water remote-sensing reflectance spectra $R_{rs}(\lambda) = L_w(\lambda)/E_d(\lambda, 0+)$ (L_w is the water-leaving radiance), was based on the knowledge of seasonal atmospheric transmittance over the APES and applying the reciprocity principle for atmospheric transmittance along the target to satellite as presented in Appendix A. Further conversion from the $R_{rs}(\lambda)$ to the under-water remote-sensing reflectance spectra $r_{rs}(\lambda)$ was performed using the equation by Craig *et al.* [29] derived from the radiative transfer simulations:

$$r_{rs}(\lambda) = \frac{R_{rs}(\lambda)}{0.52 + 1.7R_{rs}(\lambda)} \quad (4)$$

The TSS absorption coefficient at 665 nm $a_{TSS}(665)$, VSS, FSS and CDOM were then estimated by the semi-empirical underwater optical algorithm derived from the ModMon measurements [30]:

$$a_{TSS}(665) = 0.01649\,\mathrm{Chl} \quad (5)$$

$$\mathrm{VSS} = 8.300[a_{TSS}(665)]^{0.8672} \quad (6)$$

$$\mathrm{TSS} = 13.68[a_{TSS}(665)]^{0.5041} \quad (7)$$

$$\mathrm{FSS} = \mathrm{TSS} - \mathrm{VSS} \quad (8)$$

$$a_{CDOM}(412.5) = 4.791[G(665)/G(560)]^{1.218} \quad (9)$$

The non-atmospherically corrected algorithm was derived from the same database as the corrected version; without implementing the conversion from TOA radiance to Gordon's parameter *G*. Accordingly, the Chl concentration was directly related to the spectral TOA bidirectional reflectance [58] $r(\lambda, \mathrm{TOA}) = L_u(\lambda, \mathrm{TOA})/E_0(\lambda)$ ($L_u(\lambda, \mathrm{TOA})$ is the spectral upwelling radiance at the TOA and $E_0(\lambda)$ is the spectral extraterrestrial irradiance normal to the solar beam at the mean solar distance:

$$\mathrm{Chl} = 20.59[r(709, \mathrm{TOA})/r(665, \mathrm{TOA})]^{4.055} \quad (10)$$

The $a_{TSS}(665)$, VSS, TSS, and FSS were estimated by Equations (5–8), respectively, while the $a_{CDOM}(412.5)$ was estimated from the following equation:

$$a_{CDOM}(412.5) = 6.489[r(665, \mathrm{TOA})/r(560, \mathrm{TOA})]^{1.424} \quad (11)$$

Equation (11) was derived from the ModMon measured and modeling data assuming spectral reflectance ratios equality:

$$r(665, \mathrm{TOA}) / r(560, \mathrm{TOA}) = R_{\mathrm{trs}}(665, 0+) / R_{\mathrm{trs}}(560, 0+) \quad (12)$$

where $R_{\mathrm{trs}}(\lambda, 0+) = L_{\mathrm{u}}(\lambda, 0+)/E_{\mathrm{d}}(\lambda, 0+)$ is the total above-water reflectance. Equation (12) assumes that reflectance is unchanged throughout the atmosphere. Extensive observational evidences support the above assumption [13,59].

3. Results and Discussion

3.1. Validation of r_{rs} Approximations

Figure 3 shows the plot of relative errors for individual values of G at λ = 665 nm and μ_2 = 1 associated with the approximation for r_{rs} described by Equation (2) yielding R^2 = 0.99 and NRMSE = 2.1% compared to the IIM computations. Errors were between −6% and 9%, increasing nearly monotonically with μ_1 and decreasing in absolute value with G; at G = 0.56 all errors are zero. It is important to note that using the spectral G-ratios for WQCs retrievals significantly decreases errors relating to the unknown scattering phase function $p(\theta)$. For the NRE, inaccuracies associated with the $p(\theta)$ were estimated within ±1% [30].

Figure 3. Relative errors of approximate values of r_{rs} calculated relative to r_{rs} computed by the invariant imbedding method (IIM). Calculations are shown for λ = 665 nm and μ_2 = 1.

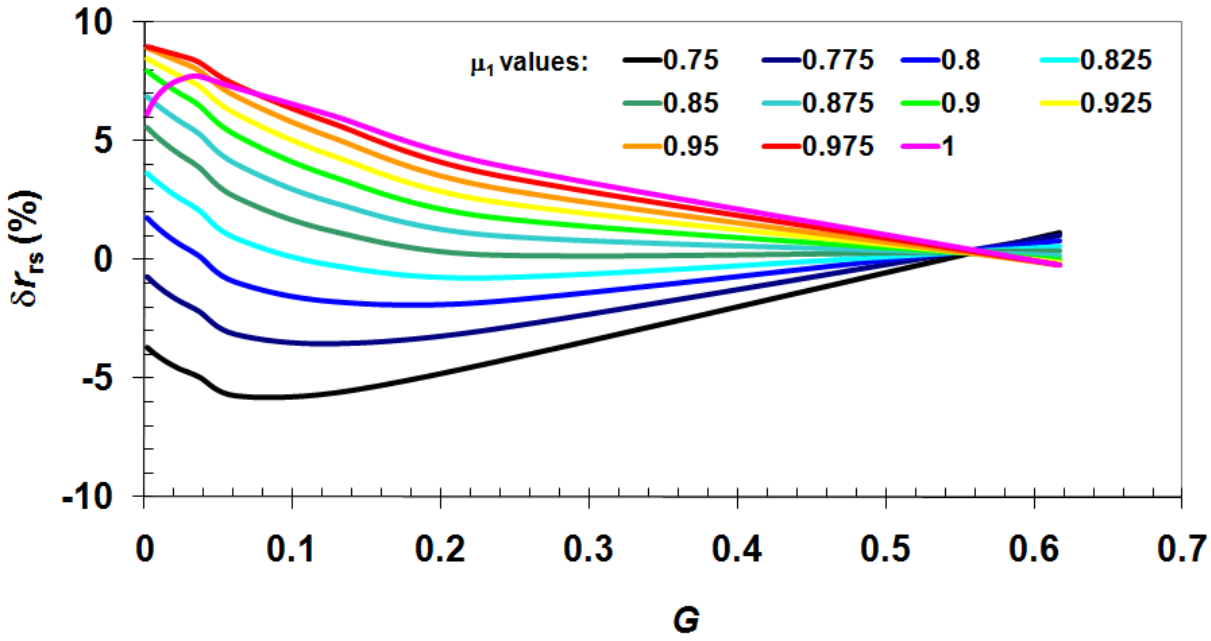

3.2. Validation of WQC Algorithms

The scatter plots comparing Chl predicted from the MERIS data with Chl measured during FerryMon trips are shown on Figure 4. Both the atmospherically corrected (Figure 4(a)) and uncorrected (Figure 4(b)) algorithms were used for Chl computations. Results demonstrated relatively good correlation and accuracy between predicted and measured values for the both the NRE and PS. Although the obtained NRMSE errors (52–75%) were greater than the suggested threshold of 35% (0.05 to 50.0 mg m^{-3}) for satellite sensors [60,61], these values may be considered as acceptable taking

into account the complexity of waters under consideration and the great daily and seasonal WQCs variability. Figure 4 illustrates that the results obtained by both remote sensing algorithms are better for Chl values >10 mg m^{-3}. This result is especially important for the purpose of detecting dates and locations of Chl exceeding 40 mg m^{-3}. The 40 mg m^{-3} value is the basis for the Total Maximum Daily Load (TMDL) nitrogen non-point source loading reductions established for the NRE [62].

Figure 4. Scatter plot for NRE (Neuse River Estuary) and Pamlico Sound (PS) Chl values comparing MERIS retrieval estimates to FerryMon measured values for both with **(a)** and without **(b)** atmospheric correction. The Chl values exceeding Total Maximum Daily Load (TMDL) values (40 mg m^{-3}) are illustrated in the upper right rectangle.

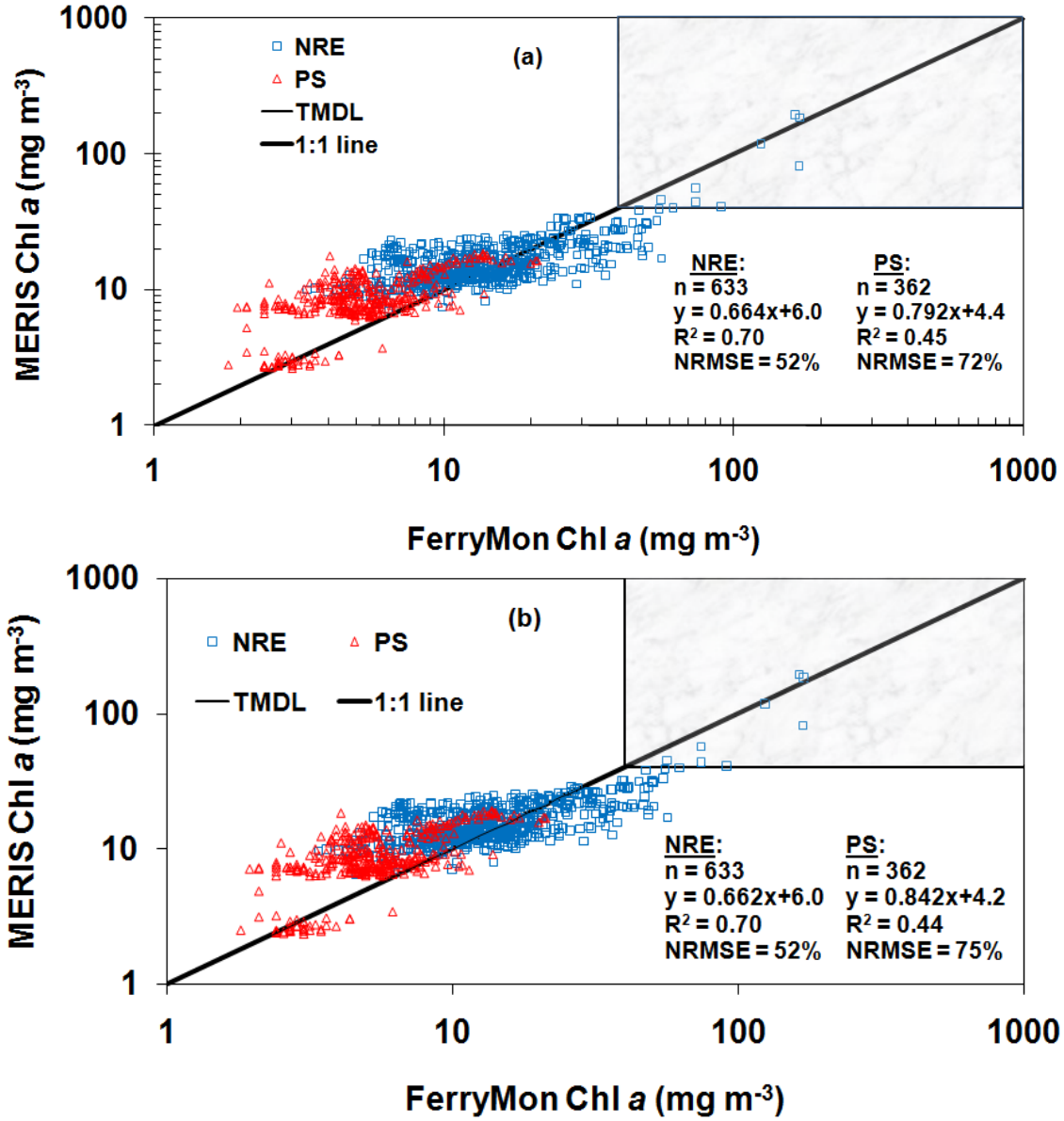

Two opposing effects had a substantial impact across the study area. First, Chl variability in the PS (52%) was significantly lower than in the NRE (94%). Second, Chl concentrations in PS were typically much lower than in the NRE (Table 1). Accordingly, results varied between systems (Figure 4). The NRMSE, R^2 and significance level (p), were better for NRE than for PS (Table 1).

It was not surprising that the Chl retrieval accuracies were similar for the both algorithms. Moreover, any attempts to apply more realistic atmospheric correction schemes, including the direct and diffuse light fluxes and aerosol light scattering simulations [46–49], resulted in even poorer results. The additional complexity associated with the atmospheric correction applied in this study, likely did not adequately represent atmospheric optical processes to the extent necessary to result in a measurable improvement in WQCs retrievals. Thus, the future investigation of real atmospheres over the NRE and PS, especially for aerosol properties, may substantially improve the atmospheric models and subsequent WQCs retrieval results for the APES.

A direct comparison between the ModMon measurements and MERIS predictions of WQCs was possible only on 14 October 2008, when ModMon and MERIS were temporally (Δt = 0.75 h) and spatially (Δd = 76 m) aligned. Table 2 contains the results derived for both remote-sensing algorithms. The errors for all WQCs (excluding FSS) closely approximated those obtained from the *in situ* water quality algorithm [30].

Table 1. Validation results of predicted (MERIS) *versus* measured (FerryMon) Chl concentrations for the Neuse River Estuary and Pamlico Sound both with (upper rows) and without (lower rows) atmospheric correction. The columns from the left to the right mean the sample size (*n*), measured mean, standard deviation (SD), coefficient of variation (CV), normalized mean biased error (NMBE), normalized root-mean-squares error (NRMSE), determination coefficient (R^2), significance level (*p*), intercept and slope.

n	Mean (mg m^{-3})	SD (mg m^{-3})	CV (%)	NMBE (%)	NRMSE (%)	R^2	*p*	Intercept (mg m^{-3})	Slope
Neuse River Estuary									
633	17.7	12.6	71	2.7	52	0.70	3×10^{-165}	6.0	0.66
633	17.8	12.4	70	2.8	52	0.70	6×10^{-165}	6.0	0.66
Pamlico Sound									
362	9.1	3.5	38	55	72	0.45	3×10^{-49}	4.4	0.79
362	9.2	3.8	41	56	75	0.44	2×10^{-47}	4.2	0.84

Table 2. Results comparing predicted (MERIS) *versus* measured (ModMon) WQCs values for NRE station #120 both with (upper row) and without (lower row) atmospheric correction. ModMon data were collected on 14 October 2008 at 09:40 AM EST and the MERIS overpass occurred at 10:25 AM EST. The numbers in parentheses are the MERIS WQCs errors relative to the ModMon data.

	Chl (mg m^{-3})	VSS(g m^{-3})	FSS(g m^{-3})	TSS(g m^{-3})	a_{CDOM}(412.5)(m^{-1})
ModMon	15.5	2.4	1.5	3.9	4.1
MERIS (with atm. correction)	11.2(−28%)	1.9(−22%)	3.9(161%)	5.8(48%)	2.8(−32%)
MERIS (without atm. correction)	10.9(−30%)	1.8(−23%)	3.9(159%)	5.7(46%)	3.2(−21%)

3.3. WQC Dynamics

Figure 5 illustrates the seasonal dynamics of WQCs in the NRE derived from the ModMon, FerryMon and MERIS datasets (2006–2009). Only MERIS pixels located within a radius of 150 m from FerryMon sampling locations for the NRE and PS routes were selected for analysis. The ModMon observations correspond to station 120. The distances between this station and selected MERIS pixels ranged between 76 and 1,546 m. Only the results of the atmospheric correction algorithm for MERIS WQCs estimates are shown in Figure 5. The non-correction algorithm had very similar results (not presented). WQCs using the algorithm described in [30] are also presented in Figure 5.

Figure 5. Seasonal dynamics of daily-averaged WQCs in NRE (2006–2009) for Chl **(a)**, VSS **(b)**, FSS **(c)**, TSS **(d)** and $a_{CDOM}(412.5)$ **(e)**. FerryMon data and TMDL line are shown only for Chl, but measured and predicted ModMon and MERIS values are shown for all WQCs.

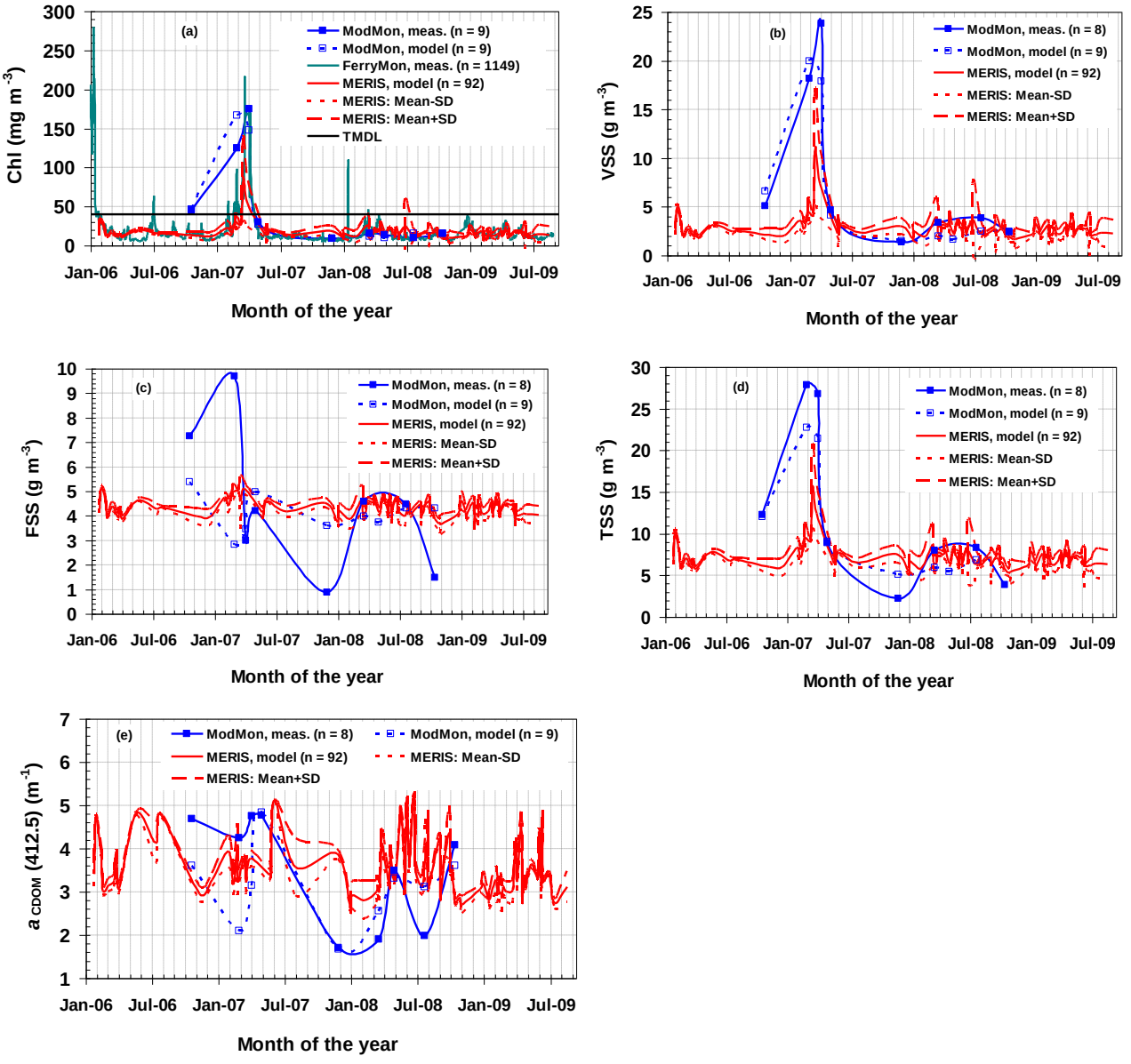

ModMon and FerryMon measurement data closely correspond with MERIS-derived observations for Chl, VSS, TSS, and $a_{CDOM}(412.5)$, but values for FSS were less encouraging (Figure 5). Figure 5 was used to identify the stable *versus* unstable water quality conditions in the NRE during different time periods. System instability is expressed by long duration (>10-day) periods of high concentrations of VSS (>6 g m^{-3}) and TSS (>11 g m^{-3}), compared to the lower background WQC values [63]. These periods were observed twice during the approximately four year study duration (2006–2009); occurring in January 2006 and February–April 2007. Less pronounced, shorter duration periods of high WQCs concentrations were also observed in July 2006 and January and March 2008. Chl peaks correspond with seasonal NRE phytoplankton blooms [64]. Due to limited collection days for ModMon and MERIS, only the February–April 2007 VSS (Figure 5(b)) and TSS (Figure 5(d)) peaks were detectable.

Figure 6. Daily-averaged values for volatile suspended solids (VSS) **(a)** and total suspended solids (TSS) **(b)** predicted from FerryMon and MERIS for the NRE (2006−2009).

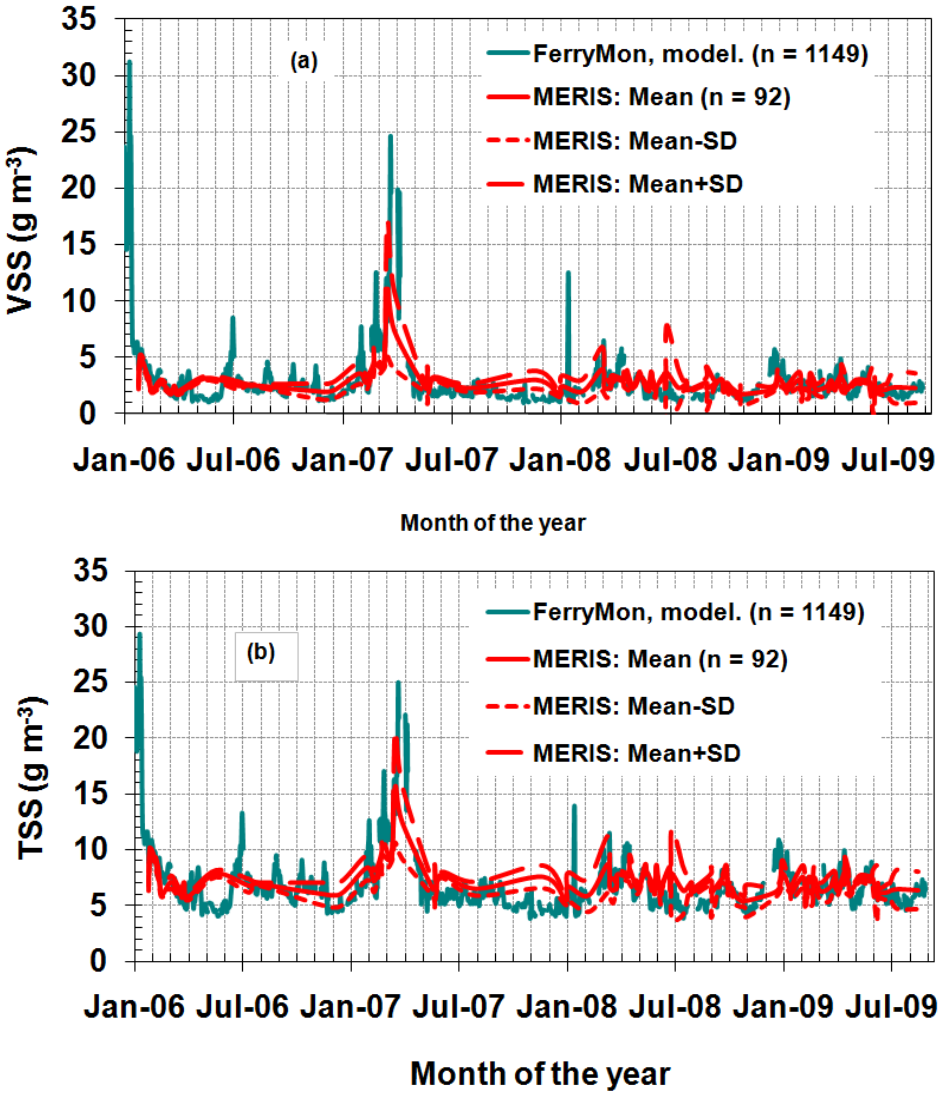

Nevertheless, the less stable VSS (Figure 6(a)) and TSS (Figure 6(b)) peaks may be discerned from the FerryMon Chl data based on relationships between Chl and particulate matter characteristic for

NRE (Equations (5–7)). The VSS and TSS peaks are also evident in the MERIS-derived estimates presented in Figure 6(a,b), respectively. A simple atmospheric correction was used for these estimates (Appendix A). Figures 5 and 6 illustrate the seasonal variability and unstable nature of the NRE WQCs.

Measured FerryMon and modeled MERIS Chl dynamics (non-atmospherically corrected) were compared for the PS area exhibited several seasonal peaks and depressions (Figure 7). The most prominent and prolonged peaks with Chl > 10 mg m^{-3}, occurred in February–March 2006, July–August 2006, and January–February 2007. Only one Chl peak, with concentrations exceeding TMDL value of 40 mg m^{-3}, was measured by FerryMon in December 2006. The dates of these peaks are very close to those observed for the NRE. Similar peaks and depressions may be expected for VSS and TSS based on the direct relationships between WQCs (Equations (5–7)).

Figure 7. The seasonal dynamics (2006–2009) of the measured FerryMon and predicted MERIS daily-averaged Chl for the PS.

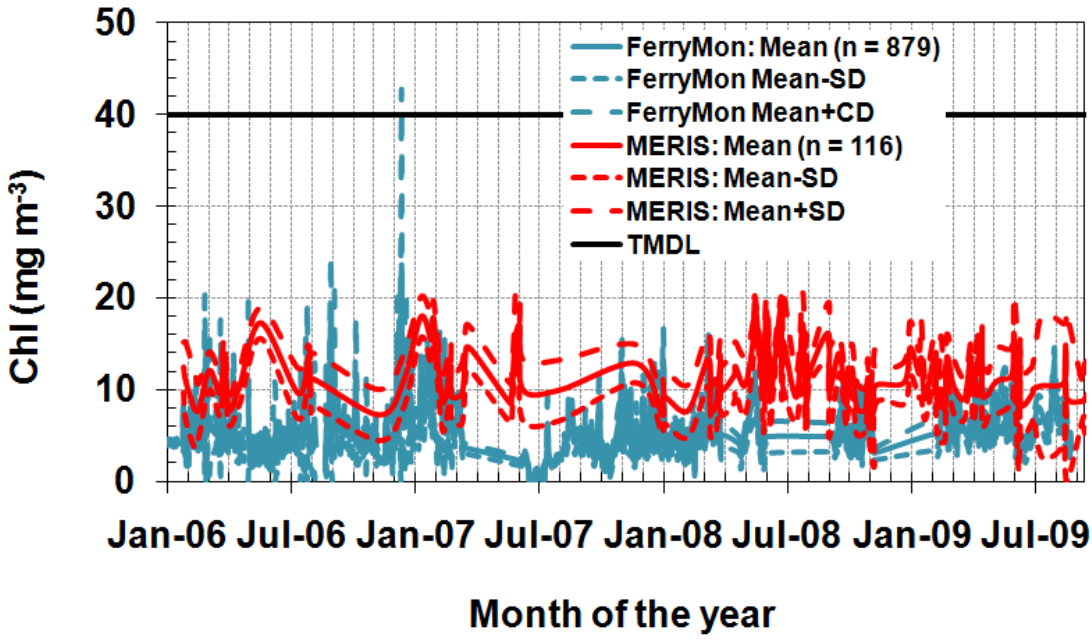

4. Conclusions

Two semi-empirical remote-sensing optical algorithms for the retrieval of WQCs in the APES were developed and validated for potential operational monitoring to complement existing *in situ* monitoring programs (ModMon and FerryMon). NRE *in situ* Chl data collected by FerryMon and remote sensing MERIS radiance data were used to develop relationships to support MERIS Chl retrieval results. The ModMon Chl, CDOM, VSS, FSS and TSS data collected in the NRE were used to develop algorithms for estimation other WQCs.

One Chl algorithm incorporated a very simple atmospheric correction based on the knowledge of seasonal atmospheric transmittance over the APES and applying the reciprocity principle for atmospheric transmittance along the target to satellite path using a modified quasi-single-scattering approximation (QSSA) for estimating the spectral Gordon's parameter and WQCs. The second algorithm estimated WQCs directly from TOA satellite spectral radiance data. Both algorithms

performed similarly in the NRE (R^2 = 0.70; NRMSE = 52%) and PS (R^2 = 0.45; NRMSE = 72%). Both algorithms facilitated a discernment of stable and unstable WQC time periods in the APES (Figures 6 and 7).

The implementation of a robust atmospheric radiative transfer model to more accurately represent the optical properties of atmospheric aerosols would be expected to significantly enhance WQCs retrieval accuracies. However, the results reported from this study indicate that reasonably good results for Chl, VSS, TSS, and $a_{CDOM}(412.5)$ retrieval can be obtained using even uncorrected MERIS imagery data. This result is particularly important due to resource limitations frequently encountered with long-term operational monitoring programs.

WQC products derived from MERIS imagery for the NRE-PS area based on algorithms presented here are available from the US Environmental Protection Agency web site for further use by environmental decision makers. Data products are available for both visualization and direct download at http://maps6.epa.gov/aptw/viewer.htm.

Acknowledgments

The US Environmental Protection Agency funded and partially conducted the research described in this paper. Although this work was reviewed by EPA and has been approved for publication, it may not necessarily reflect official Agency policy. Mention of any trade names or commercial products does not constitute endorsement or recommendation for use. The authors would like to thank Alexander Kokhanovsky for making available the results of his radiative transfer calculations and Jayantha Ediriwickrema for his algorithm implementation and imagery processing support. Funding for this study was provided by EPA's Office of Research and Development (ORD) and the Global Earth Observation System of Systems (GEOSS) program's Advanced Monitoring Initiative (AMI Grant #14). MERIS imagery data was provided by the European Space Administration under a MERIS Principal Investigator initiated proposal (#4698). ModMon and FerryMon water quality monitoring/assessment programs were supported by the North Carolina Department of Environment and Natural Resources, Division of Water Quality, and the National Science Foundation (Environmental Engineering, Biological and Chemical Oceanography Programs).

References

1. Boss, E.; Perry, M.J.; Swift, D.; Taylor, L.; Brickley, P.; Zaneveld, J.R.V. Three years of ocean data from a bio-optical profiling float. *Eos Trans. AGU* **2008**, *89*, 209–210.
2. Campbell, J.W.; Esaias, W.E. Basis for spectral curvature algorithms in remote sensing of chlorophyll. *Appl. Opt.* **1983**, *22*, 1084–1093.
3. O'Reilly, J.E.; Maritorena, S.; Mitchell, B.G.; Siegel, D.A.; Carder, K.L.; Garver, S.A.; Kahru, M.; McClain, C. Ocean color chlorophyll algorithms for SeaWiFS. *J. Geophys. Res.* **1998**, *103*, 24937–24953.
4. Dall'olmo, G.; Gitelson, A.A. Effect of bio-optical parameter variability on the remote estimation of chlorophyll-a concentration in turbid productive waters: Experimental results. *Appl. Opt.* **2005**, *44*, 412–422.

5. IOCCG. *Remote Sensing of Inherent Optical Properties: Fundamentals, Tests of Algorithms, and Applications*; Reports of the International Ocean-Colour Coordinating Group, No. 5; Lee, Z., Ed.; IOCCG: Dartmouth, NS, Canada, 2006.
6. Khorram, S.; Cheshire, H.M. Remote sensing of water quality in the Neuse River Estuary, North Carolina. *Photogramm. Eng. Remote Sensing* **1985**, *51*, 329–341.
7. Woodruff, D.L.; Stumpf, R.P.; Scope, J.A.; Paerl, H.W. Remote estimation of water clarity in optically complex estuarine waters. *Remote Sens. Environ.* **1999**, *68*, 41–52.
8. Stumpf, R.P.; Pennock, J.R. Remote estimation of the diffuse attenuation coefficient in a moderately turbid estuary. *Remote Sens. Environ.* **1991**, *38*, 183–191.
9. Gordon, H.R. Simple calculation of the diffuse reflectance of ocean. *Appl. Opt.* **1973**, *12*, 2803–2804.
10. Haltrin, V.I.; Gallegos, S.C. About nonlinear dependence of remote sensing and diffuse reflection coefficients of Gordon's parameter. In *Proceedings of Conference "Current Problems in Optics of Natural Waters"*, St. Petersburg, Russia, 8–12 September 2003; pp. 363–369. Available online: http://vih.freeshell.org/pp/03_ONW_St.Petersburg/Nonlin_RSR.pdf (accessed on 28 March 2011).
11. Sokoletsky, L. A comparative analysis of simple radiative transfer approaches for aquatic environments. In *Proceedings of the* 2004 *ENVISAT & ERS Symposium*, Salzburg, Austria, 6–10 September 2004; [CD-ROM].
12. Twardowski, M.S.; Boss, E.; Macdonald, J.B.; Pegau, W.S.; Barnard, A.H.; Zaneveld, J.R.V. A model for estimating bulk refractive index from the optical backscattering ratio and the implications for understanding particle composition in case I and case II waters. *J. Geophys. Res.* **2001**, *106*, 14129–14142.
13. Sokoletsky, L. *In situ* and Remote Sensing Bio-optical Methods for the Estimation of Phytoplankton Concentration in the Gulf of Aqaba (Eilat). Ph.D. Thesis, Bar-Ilan University, Ramat-Gan, Israel, 2003.
14. Woźniak, S.B.; Stramski, D. Modeling the optical properties of mineral particles suspended in seawater and their influence on ocean reflectance and chlorophyll estimation from remote sensing algorithms. *Appl. Opt.* **2004**, *43*, 3489–3503.
15. Karaska, M.A.; Huguenin, R.L.; Beacham, J.L.; Wang, M.; Jensen, J.R.; Kaufmann, R.S. AVIRIS measurements of chlorophyll, suspended minerals, dissolved organic carbons, and turbidity in the Neuse River, North Carolina. *Photogramm. Eng. Remote Sensing* **2004**, *70*, 125–133.
16. Huguenin, R.L.; Wang, M.; Biehl, R.; Stoodley, S.; Rogers, J.N. Automated subpixel photobathymetry and water quality mapping. *Photogramm. Eng. Remote Sensing* **2004**, *70*, 111–123.
17. Morel, A.; Prieur, L. Analysis of variations in ocean color. *Limnol. Oceanogr.* **1977**, *22*, 709–722.
18. Dekker, A.G.; Peters, S.W.M. The use of the Thematic Mapper for the analysis of eutrophic lakes: A case study in the Netherlands. *Int. J. Remote Sens.* **1993**, *14*, 799–821.
19. Kalio, K.; Kutser, T.; Hannonen, T.; Koponen, S.; Pulliainen, J.; Vepsäläinen, J.; Pyhälahti, T. Retrieval of water quality from airborne imaging spectrometry of various lake types in different seasons. *Sci. Total Environ.* **2001**, *268*, 59–77.

20. Doxaran, D.; Froidefond, J.M.; Castaing, P. A reflectance band ratio used to estimate suspended matter concentrations in sediment-dominated coastal waters. *Int. J. Remote Sens.* **2002**, *23*, 5079–5085.
21. Brezonik, P.; Menken, K.D.; Bauer, M. Landsat-based remote sensing of lake water quality characteristics, including chlorophyll and colored dissolved organic matter (CDOM). *Lake Reserv. Manag.* **2005**, *4*, 373–382.
22. Morel, A.; Gentili, B. A simple band ratio technique to quantify the colored and detrital organic material from ocean color remotely sensed data. *Remote Sens. Environ.* **2009**, *113*, 998–1011.
23. Sokoletsky, L.; Gallegos, S. Towards development of an improved technique for remote retrieval of water quality components: An approach based on the Gordon's parameter spectral ratio. In *Proceedings of the Ocean Optics XX Conference*, Anchorage, AK, USA, 27 September–1 October 2010; #100881.
24. Ruddick, K.G.; Gons, H.J.; Rijkeboer, M.; Tilstone, G. Optical remote sensing of chlorophyll *a* in case 2 waters by use of an adaptive two-band algorithm with optimal error properties. *Appl. Opt.* **2001**, *40*, 3575–3585.
25. Gons, H.J.; Rijkeboer, M.; Ruddick, K.G. A chlorophyll-retrieval algorithm for satellite imagery (Medium Resolution Imaging Spectrometer) of inland and coastal waters. *J. Plankton Res.* **2002**, *24*, 947–951.
26. Lee, Z.P.; Carder, K.L.; Arnone, R.A. Deriving inherent optical properties from water color: A multiband quasi-analytical algorithm for optically deep waters. *Appl. Opt.* **2002**, *41*, 5755–5772.
27. Peters, S.W.M.; Pasterkamp, R.; van de Woerd, H.J. A sensitivity analysis of analytical inversion methods to derive chlorophyll from MERIS spectra in case-II waters. In *Proceedings of the Ocean Optics XVI Conference*, Santa Fe, NM, USA, November 2002; pp. 363–369. Available online: http://www.brockmann-consult.de/revamp/pdfs/147.pdf (accessed on 28 March 2011).
28. Cauwer, V.D.; Ruddick, K.; Park, Y.J.; Kyramarios, M. Optical remote sensing in support of eutrophication monitoring in the Southern North Sea. *EARSeL eProceedings* **2004**, *3*, 208–221.
29. Craig, S.E.; Lohrenz, S.E.; Lee, Z.P.; Mahoney, K.L.; Kirkpatrick, G.J.; Schofield, O.M.; Steward, R.G. Use of hyperspectral remote sensing reflectance for detection and assessment of the harmful alga, *Karenia brevis*. *Appl. Opt.* **2006**, *45*, 5414–5425.
30. Sokoletsky, L.G.; Lunetta, R.S.; Wetz, M.S.; Paerl, H.W. Assessment of the water quality components in turbid estuarine waters based on radiative transfer approximations. **2011**, submitted.
31. Defoin-Platel, M.; Chami, M. How ambiguous is the inverse problem of ocean color in coastal waters? *J. Geophys. Res.* **2007**, *112*, C03004, doi:10.1029/2006JC003847.
32. Lunetta, R.S.; Knight, J.F.; Paerl, H.W.; Streicher, J.J.; Peierls, B.L.; Gallo, T.; Lyon, J.G.; Mace, T.H.; Buzzelli, C.P. Measurement of water colour using AVIRIS imagery to assess the potential for an operational monitoring capability in the Pamlico Sound Estuary, USA. *Int. J. Remote Sens.* **2009**, *30*, 3291–3314.
33. Berk, A.; Bernstein, L.S.; Robertson, D.C. *MODTRAN: A Moderate Resolution Model for LOWTRAN 7*; Technical Report GL-TR-0122; AFGL, Hanscom AFB: Bedford, MA, USA, 1989.
34. Stamnes, K.; Conklin, P. A new multi-layer discrete ordinate approach to radiative transfer in vertically inhomogeneous atmospheres. *J. Quant. Spectrosc. Radiat. Transfer* **1984**, *31*, 273–282.

35. Paerl, H.W.; Bales, J.D.; Ausley, L.W.; Buzzelli, C.P.; Crowder, L.B.; Eby, L.A.; Fear, J.M.; Go, M.; Peierls, B.L.; Richardsoni, T.L.; Ramus, J.S. Ecosystem impacts of three sequential hurricanes (Dennis, Floyd, and Irene) on the United States' largest lagoonal estuary, Pamlico Sound, NC. *Proc. Nat. Acad. Sci. USA* **2001**, *98*, 5655–5660.
36. Paerl, H.W.; Valdes, L.M.; Joyner, A.R.; Peierls, B.L.; Piehler, M.F.; Riggs, S.R.; Christian, R.R.; Eby, L.A.; Crowder, L.B.; Ramus, J.S.; Clesceri, E.J.; Buzzelli, C.P.; Luettich, R.A. Ecological response to hurricane events in the Pamlico Sound system, North Carolina, and implications for assessment and management in a regime of increased frequency. *Estuar. Coast.* **2006**, 29, 1033–1045.
37. Burkholder, J.; Eggleston, D.; Glasgow, H.; Brownie, C.; Reed, R.; Janowitz, G.; Posey, M.; Melia, G.; Kinder, C.; Corbett, R.; Toms, D.; Alphin, T.; Deamer, N.; Springer, J. Comparative impacts of two major hurricane seasons on the Neuse River and western Pamlico Sound ecosystems. *Proc. Nat. Acad. Sci. USA* **2004**, *101*, 9291–9296.
38. Copeland, B.J.; Gray, J. *Status and Trends of the Albemarle-Pamlico Estuary Study*; Technical Report 90-01; Department of Environment, Health, and Natural Resources, NC State University: Raleigh, NC, USA, 1991.
39. Paerl, H.W.; Pinckney, J.L.; Fear, J.M.; Peierls, B.L. Ecosystem responses to internal and watershed organic matter loading: consequences for hypoxia in the eutrophying Neuse River Estuary, North Carolina, USA. *Mar. Ecol. Prog. Ser.* **1998**, *166*, 17–25.
40. Paerl, H.W.; Valdes, L.M.; Piehler, M.F.; Stow, C.A. Assessing the effects of nutrient management in an estuary experiencing climatic change: The Neuse River Estuary, NC, USA. *Environ. Manage.* **2006**, *37*, 422–436.
41. Buzzelli, C.P.; Ramus, J.R.; Paerl, H.W. Ferry-based monitoring of surface water quality in North Carolina estuaries. *Estuaries* **2003**, *26*, 975–984.
42. Mobley, C.D. Estimation of the remote-sensing reflectance from above-surface measurements. *Appl. Opt.* **1999**, *38*, 7442–7455.
43. Sokoletsky, L. Comparative analysis of selected radiative transfer approaches for aquatic environments. *Appl. Opt.* **2005**, *44*, 136–148.
44. Paerl, H.W.; Rossignol, K.L.; Hall, N.S.; Guajardo, R.; Joyner, A.R.; Peierls, B.L.; Ramus, J.S. FerryMon: Ferry-based monitoring and assessment of human and climatically-driven environmental change in the Pamlico Sound System, North Carolina, USA. *Environ. Sci. Technol.* **2009**, *43*, 7609–7613.
45. Curran, P.J.; Steele, C.M. MERIS: The re-branding of an ocean sensor. *Int. J. Remote Sens.* **2005**, *26*, 1781–1798.
46. Gordon, H.R.; Castaño, D.J. Coastal Zone Color Scanner atmospheric correction algorithm: Multiply scattering effects. *Appl. Opt.* **1987**, *26*, 2111–2122.
47. Haltrin, V.I. Empirical relationship between aerosol scattering phase function and optical thickness of atmosphere above the ocean. *Proc. SPIE* **1998**, *3433*, 334–342.
48. Gong, S.; Huang, J.; Li, Y.; Wang, H. Comparison of atmospheric correction algorithms for TM image in inland waters. *Int. J. Remote Sens.* **2008**, *29*, 2199–2210.

49. Katsev, I.L.; Prikhach, A.S.; Zege, E.P.; Ivanov, A.P.; Kokhanovsky, A.A. Iterative procedure for retrieval of spectral aerosol optical thickness and surface reflectance from satellite data using fast radiative code and its application to MERIS measurements. In *Satellite Aerosol Remote Sensing over Land*; Kokhanovsky, A.A., de Leeuw, G., Eds.; Springer-Praxis: Berlin, Germany, 2009; pp. 101–134.
50. Albert, A.; Gege, P. Inversion of irradiance and remote sensing reflectance in shallow water between 400 and 800 nm for calculations of water and bottom properties. *Appl. Opt.* **2006**, *45*, 2331–2343.
51. Mishchenko, M.I.; Dlugach, J.M.; Yanovitskij, E.G.; Zakharova, N.T. Bidirectional reflectance of flat, optically thick particulate layers: An efficient radiative transfer solution and applications to snow and soil surfaces. *J. Quant. Spectrosc. Radiat. Transfer* **1999**, *63*, 409–432.
52. Kokhanovsky, A.A.; Sokoletsky, L.G. Reflection of light from semi-infinite absorbing turbid media. Part 1: Spherical albedo. *Color Res. Appl.* **2006**, *31*, 491–497.
53. Kokhanovsky, A.A.; Sokoletsky, L.G. Reflection of light from semi-infinite absorbing turbid media. Part 2: Plane albedo and reflection function. *Color Res. Appl.* **2006**, *31*, 498–509.
54. Sokoletsky, L.G.; Nikolaeva, O.V.; Budak, V.P.; Bass, L.P.; Lunetta, R.S.; Kuznetsov, V.S.; Kokhanovsky, A.A. Comparison of different numerical and analytical solutions of the radiative-transfer equation for plane albedo with emphasis on the natural waters consideration. *J. Quant. Spectrosc. Radiat. Transfer* **2009**, *110*, 1132–1146.
55. Petzold, T.J. *Volume Scattering Functions for Selected Ocean Waters*; Technical Report SIO 72-78; Scripps Institution of Oceanography: San Diego, CA, USA, 1972.
56. Haltrin, V.I. An analytical Fournier-Forand scattering phase function as an alternative to the Henyey-Greenstein phase function in hydrologic optics. *Proc. IEEE* **1998**, *11*, 910–913.
57. Mobley, C.D.; Sundman, L.K.; Boss, E. Phase function effects on oceanic light fields. *Appl. Opt.* **2002**, *41*, 1035–1050.
58. Hapke, B. *Theory of Reflectance and Emittance Spectroscopy*; Cambridge University Press: New York, NY, USA, 1993.
59. Knaeps, E.; Sterckx, S; Raymaekers, D. A seasonally robust empirical algorithm to retrieve suspended sediment concentrations in the Scheldt River. *Remote Sens.* **2010**, *2*, 2040–2059.
60. Hooker, S.B.; Esaias, W.E.; Feldman, G.C.; Gregg, W.W.; McClain, C.R. An overview of SeaWiFS and ocean color. In *SeaWiFS Technical Report Series, NASA Technical Memorandum* 104566; Hooker, S.B., Firestone, E.R., Eds.; NASA Goddard Space Flight Center: Greenbelt, MD, USA, 1992; Volume 1, pp. 1–24.
61. Mueller, J.L.; Austin, R.W.; Fargion, G.S.; McClain, C.R. Ocean color radiometry and bio-optics. In *Ocean Optics Protocols for Satellite Ocean Color Sensor Validation*; Mueller, J.L., Fargion, G.S., Eds.; NASA/TM-2003-21621, Revision 4; NASA Goddard Space Flight Center: Greenbelt, MD, USA, 2003; Volume 1.
62. Borsuk, M.E.; Stow, C.A.; Reckhow, K.H. Integrated approach to Total Maximum Daily Load development for Neuse River Estuary using Bayesian Probability Network Model (Neu-BERN). *J. Water Res. Plan. Manage*. **2003**, *131*, 271–282.

63. Smith, E.T.; Zhang, H.X. Developing key water quality indicators for sustainable water resources management. In *Proceedings of 77th Annual Water Environment Federation Technical Exhibition and Conference*, New Orleans, LA, USA, 2–6 October 2004. Available online: http://acwi.gov/swrr/Rpt_Pubs/WEFTEC04_SWRR_Zhang.pdf (accessed on 28 March 2011).
64. Rigollier, C.; Bauer, O.; Wald, L. On the clear sky model of the 4th European Solar Radiation Atlas with respect to the Heliosat method. *Solar Energy* **2000**, *68*, 33–48.
65. Aboura, R.; Lansari, A. Satellite-derived surface radiation budget over the Algerian area. In *Proceedings of the International Congress on Photovoltaic and Wind Energy (ICPWE'03)*, Tlemcen, Algeria, 16–18 December 2003. Available online: http://www.cder.dz/download/Art02.pdf (accessed on 28 March 2011).
66. Remund, J.; Wald, L.; Lefèvre, M.; Ranchin, T.; Page, J. Worldwide linke turbidity information. In *Proceedings of the ISES Solar World Congress*, Göteborg, Sweden, 16–19 June 2003. Available online: http://www.meteotest.ch/fileadmin/user_upload/Sonnenenergie/pdf/Remund_ises2003_linketurbidity.pdf (accessed on 28 March 2011).
67. Remund, J.; Kunz, S.; Schilter, C. *Handbook of METEONORM, version 6.114. Part II: Theory*; METEOTEST: Bern, Switzerland, 2009. Available online: http://www.meteonorm.com/media/pdf/mn6_theory.pdf (accessed on 28 March 2011).
68. Spencer, J.W. Fourier series representation of the position of the sun. *Search* **1971**, *2*, 272.
69. Kasten, F.; Young, A.T. Revised optical air mass tables and approximation formula. *Appl. Opt.* **1989**, *28*, 4735–4738.
70. Exell, R.H.B. A mathematical model for solar radiation in South-East Asia (Thailand). *Solar Energy* **1981**, *26*, 161–168.
71. Duffie, J.A.; Beckman, W.A. *Solar Engineering of Thermal Processes*; Wiley: New York, NY, USA, 1991.
72. Helyar, A.G. Equation of time. 2001. Available online: http://homepages.pavilion.co.uk/aghelyar/sundat.htm (accessed on 28 March 2011).
73. Sekera, Z. Reciprocity relations for diffuse reflection and transmission of radiative transfer in the planetary atmosphere. *Astrophys. J.* **1970**, *162*, 3–16.
74. Yang, H.; Gordon, H.R. Remote sensing of ocean color: assessment of water-leaving radiance bidirectional effects on atmospheric diffuse transmittance. *Appl. Opt.* **1997**, *36*, 7887–7897.
75. Thuillier, G.; Herse, M.; Simon, P.C.; Labs, D.; Mandel, H.; Gillotay, D.; Foujols, T. The solar spectral irradiance from 200 to 2400 nm as measured by the SOLSPEC spectrometer from the ATLAS 1-2-3 and EURECA missions. *Solar Phys.* **2003**, *214*, 1–22.
76. Toole, D.A.; Siegel, D.A.; Menzies, D.W.; Neumann, M.J.; Smith, R.C. Remote-sensing reflectance determinations in the coastal ocean environment: Impact of instrumental characteristics and environmental variability. *Appl. Opt.* **2000**, *39*, 456–469.
77. Sokoletsky, L.G.; Oren, A.; Stambler, N.; Iluz, D. Practical algorithms for remote-sensing retrieval of the water column constituents in the Israeli waters. In *Proceedings of Conference "Current Problems in Optics of Natural Waters"*, St. Petersburg, Russia, 8–12 September 2009.
78. Ruddick, K.G.; Cauwer, V.D.; Park, Y.J. Seaborne measurements of near infrared water-leaving reflectance: The similarity spectrum for turbid waters. *Limnol. Oceanogr.* **2006**, *51*, 1167–1179.

Appendix A

Atmospheric Correction Equations

Atmospheric corrections were performed by first estimating the atmospheric transmittance from the sun to the target $T_{\text{down}}(\mu_0) = E_{\text{d}}(0+, \mu_0) / E_{\text{d}}(TOA, \mu_0)$, where $E_{\text{d}}(0+)$ and $E_{\text{d}}(\text{TOA})$ are the spectrally-averaged total irradiance at the surface (including diffuse sky $E_{\text{d, dif}}(0+)$ and direct sky $E_{\text{d, dir}}(0+)$ irradiances) and the top of atmosphere (TOA) levels, respectively. This step incorporated the procedure derived from [64–67] as follows:

$$E_{\text{d}}(\text{TOA}) = E_0 \varepsilon \mu_0 \tag{A1}$$

where E_0 is the solar constant (1,367 Wm^{-2}), representing the extraterrestrial irradiance normal to the solar beam at the mean solar distance; ε is the correction factor used to allow for the variation of sun-earth distance from its mean value; and μ_0 is the cosine of the solar zenith angle:

$$E_{\text{d}}(0+) = E_{\text{d, dif}}(0+) + E_{\text{d, dir}}(0+) \tag{A2}$$

$$E_{\text{d, dif}}(0+) = E_0 \varepsilon F_{\text{d}} T_{\text{rd}} \tag{A3}$$

$$E_{\text{d, dir}}(0+) = E_0 \varepsilon \mu_0 \exp(-0.8662 m \tau_{\text{R}} T_{\text{L}}) \tag{A4}$$

Here T_{L} is the Linke turbidity factor for an air mass equal to 2; $F_{\text{d}}(\mu_0, T_{\text{L}})$ is the diffuse solar zenith function which adjusts the diffuse zenith transmittance $T_{\text{rd}}(T_{\text{L}})$ to the actual solar zenith angle $\theta_0 = \arccos \mu_0$; m is the relative optical air mass; and $\tau_{\text{R}}(m)$ is the integrated Rayleigh optical thickness.

The earth-sun distance factor ε as given by Spenser [68]:

$$\varepsilon = 1.00011 + 0.034221 \cos\varphi + 0.00128 \sin\varphi + 0.000719 \cos 2\varphi + 0.000077 \sin 2\varphi \tag{A5}$$

where the day angle φ (in radians) is represented by the day of the year D (beginning on 1 January):

$$\varphi = \frac{2\pi(D-1)}{365} \tag{A6}$$

The expressions for calculation of F_{d} and T_{rd} were taken from Remund *et al.* [67]:

$$F_d = A_0 + A_1 \mu_0 + A_2 \mu_0^2 \tag{A7}$$

$$A_0 = 0.26463 - 0.061581 T_{\text{L}} + 0.0031408 T_{\text{L}}^2 \tag{A8}$$

$$A_1 = 2.04020 + 0.018945 T_{\text{L}} - 0.011161 T_{\text{L}}^2 \tag{A9}$$

$$A_2 = -1.33025 + 0.03231 T_{\text{L}} + 0.0085079 T_{\text{L}}^2 \tag{A10}$$

$$T_{rd} = -0.015843 + 0.030543 T_{\text{L}} + 0.0003797 T_{\text{L}}^2 \tag{A11}$$

The relative optical air mass for normal atmosphere was calculated by equation of Kasten and Young [69] as modified by Remund *et al.* [67] for the solar altitude angle corrected for the atmospheric refraction (in radians) $\gamma_0^{\text{refr}} = \pi/2 - \theta_0^{\text{refr}}$:

$$m = \frac{1}{\sin \gamma_0^{\text{refr}} + 0.50572(57.29578\gamma_0^{\text{refr}} + 6.07995)^{-1.6364}} \tag{A12}$$

where γ_0^{refr} is related with the uncorrected solar altitude angle $\gamma_0 = \pi/2 - \theta_0$ by:

$$\gamma_0^{\text{refr}} = \gamma_0 + 0.061359 \frac{0.1594 + 1.1230\gamma_0 + 0.065656\gamma_0^2}{1 + 28.9344\gamma_0 + 277.3971\gamma_0^2} \tag{A13}$$

The integrated Rayleigh optical thickness was calculated as follows [66]:

$$\tau_{\text{R}} = \left(6.625928 + 1.92969m - 0.170073m^2 + 0.011517m^3 - 0.000285m^4\right)^{-1} \tag{A14}$$

The month values of T_{L} were derived by linear interpolation between the values of this parameter for sites closest to the study area (Raleigh and Cove) listed in [66]. The calculation of θ_0 was carried out using the standard astronomical formulae [70,71] with the equation of time (EqT, in minutes) derived from Helyar [72] in the form:

$$\begin{aligned} \text{EqT} = &-0.025 + 0.4079\cos(T) - 7.394\sin(T) - 3.297\cos(2T) - 9.359\sin(2T) \\ &- 0.1371\cos(3T) - 0.2365\sin(3T) - 0.1588\cos(4T) - 0.1604\sin(4T) \end{aligned} \tag{A15}$$

where parameter T is related with the day angle φ by $T = (365/366)\varphi$. The Equation (A15) yields the accuracy ±0.08 minutes comparing with the very precise astronomical data.

The estimation of atmospheric transmittance $T_{\text{up}}(\mu_v) = L_{\text{u}}(\text{TOA}, \mu_v)/L_{\text{u}}(0+, \mu_v)$ along the path from the target to the satellite under direction μ_{v} was performed using reciprocity principle for atmosphere [73,74]:

$$T_{\text{up}}(\mu_v) = \left[T_{\text{down}}(\mu_0)\right]^{\mu_0/\mu_v} \tag{A16}$$

Conversion to the spectral atmospheric quantities was realized using the TOA downwelling irradiance:

$$E_{\text{d}}(\lambda, \text{TOA}, D, \mu_0) = E_0(\lambda)\varepsilon(D)\mu_0 \tag{A17}$$

where the extraterrestrial irradiance $E_0(\lambda)$ normal to the solar beam at the mean solar distance was estimated applying a fourth order polynomial interpolation for 350–800 nm spectral range of $E_0(\lambda)$ values [75]:

$$E_0(\lambda) = -3274.2 + 21.61\lambda - 0.04928\lambda^2 + 4.892\times10^{-5}\lambda^3 - 1.809\times10^{-8}\lambda^4 \tag{A18}$$

This equation yields values of 185.3, 152.2, and 139.2 μW cm^{-2} nm^{-1} for 560, *665*, and 709 nm, respectively.

The spectral above-water total reflectance was determined as:

$$R_{\text{trs}}(\lambda, 0+, D, \mu_0, \mu_v) = \frac{r(\lambda, \text{TOA}, \mu_v)}{T_{\text{down}}(\mu_0)T_{\text{up}}(\mu_v)\varepsilon(D)\mu_0} \tag{A19}$$

where $r(\lambda, \text{TOA}, \mu_v) = L_{\text{u}}(\lambda, \text{TOA}, \mu_v)/E_0(\lambda)$ is the spectral TOA bidirectional reflectance. The above-water reflectance $R_{\text{rs}}(\lambda)$ was calculated as [76, 77]:

$$R_{\text{rs}}(\lambda) = R_{\text{trs}}(\lambda, 0+) - 6.584\rho_{\text{sky}}\exp(-0.01075\lambda) \tag{A20}$$

where sky reflectance $\rho_{\text{sky}}(0+, W)$ was estimated as a function of the wind speed W (in m/sec) [78]:

$$\rho_{sky} = 0.0256 + 0.00039W + 0.000034W^2 \quad \text{(A21)}$$